Finite Fault Inversion of Mw4.1 and its Implications for Induced Earthquake Ruptures.

Colin Pennington[1], Takahiko Uchide[2], and Xiaowei Chen[1]

[1]School of Geosciences, the University of Oklahoma, Norman, OK
[2]Geological Survey of Japan, National Institute of Advanced Industrial Science and Technology (AIST), Tsukuba, Japan,

Key Points:

- A finite-fault slip model is obtained for a 2015 M_w 4.1 earthquake that occurred near Guthrie, Oklahoma.
- Both past seismicity and injection affect the observed heterogeneous slip pattern of the M_w 4.1 earthquake.
- Faults in Oklahoma exhibit more heterogeneous slip compared to similar sized earthquake in plate boundary regions.

Corresponding author: Colin Pennington , `Colin.N.Pennington@ou.edu`

Abstract

To better quantify how injection, prior seismicity and fault properties control rupture growth and propagation of induced earthquakes, we perform finite-fault slip inversion on a M_w 4.1 earthquake that occurred in April 2015, which is the largest earthquake of an induced sequence near Guthrie, Oklahoma. The slip inversion reveals a complex rupture with multiple slip patches that are anti-correlated to the cumulative slip distributions of prior seismicity. This indicates that the M_w 4.1 earthquake likely ruptured relatively strong asperities, while earlier seismicity driven by pore pressure occurred in weaker area. Compared to similar magnitude events in swarms from other regions, intraplate earthquakes in Oklahoma have higher number of well separated slip patches, indicating a difference in fault characteristics between regions. These observations suggest that both pore pressure perturbations, earthquake interactions, and fault characteristics control rupture propagation in moderate size earthquakes in Oklahoma, with the latter likely the dominant factor.

Plain Language Summary

Earthquake rupture initiates at a single point and can grow into a very large event, and the events final size is strongly affected by the heterogeneity within the fault system. Understanding how the rupture growth of induced intraplate earthquakes differs from interplate ones is important to the proper estimation of hazard. To better understand the factors that control the rupture and eventual size of earthquakes in Oklahoma we examine the rupture process of a Mw 4.1 earthquake from an earthquake sequence near Guthrie, Oklahoma. Using seismic data, we calculate the slip pattern for the event and find that a majority of slip occurs on four distinct slip patches, that are outlined by past seismicity triggered by pore pressure changes from nearby injection wells. The slip patches that failed in this rupture likely represent the strongest locked portion of the fault that were pushed to a critical state through both pore pressure and past seismicity. When comparing the rupture processes of Oklahoma earthquakes to earthquakes of a similar size in other regions those in Oklahoma have a larger number of small slip patches. This suggests that fault zone properties in Oklahoma produce more heterogeneous distributions of asperities than in other regions.

1 Introduction

The central United States has experienced a significant increase in seismicity rates since 2009, which has been largely attributed to wastewater injection (Ellsworth, 2013; Keranen et al., 2014). It is well understood that the stress perturbations produced from wastewater injection reactivate pre-existing faults, which leads to an increase in earthquake occurrence. Fault structure, stress changes due to injection, and stress interactions between earthquakes play major roles in the spatiotemporal evolution of individual sequences (M. Brown & Ge, 2018; Pennington & Chen, 2017; Qin et al., 2018; Sumy et al., 2014). What is not well understood is how these factors affect the nucleation and rupture growth of future earthquakes within individual induced earthquake sequences. Investigation of their roles in controlling the propagation of future ruptures in a sequence is needed to not just better understand the underlying physics that govern rupture growth, but also the proper assessment of seismic hazard.

Previous investigations of coseismic slip for induced earthquakes have observed both spatial and temporal phases in slip growth. The 2011 Prague earthquake contained multiple slip patches (Sun & Hartzell, 2014), and rupture models of the 2016 Pawnee earthquake showed multiple peaks of slip and moment release (Grandin et al., 2017; Moschetti et al., 2019). Previous studies have shown that the nucleation of these events was affected by prior seismicity and injection, so these two factors could play a role in these events rupture processes (Sumy et al., 2014; Pennington & Chen, 2017; Chen et al., 2017; Norbeck & Horne, 2016). Due to lack of significant prior seismicity on the fault plane for both of these events, it makes it difficult to assess the relationship between prior seismicity and coseismic slip. Moreover, an examination by Moschetti et al. (2019) of the Pawnee earthquake did not find agreement between modeled pore pressure change along the fault and the location of its slip patches. On the other hand, the non-induced intraplate 2011 M_w 5.8 Mineral Virginia earthquake also has multiple slip patches (Hartzell et al., 2013). This indicates that the fault properties of these long dormant faults might also play an important role controlling coseismic slip patterns.

To better quantify how pore pressure and earthquake interactions effect earthquake rupture propagation, we examine the largest earthquake (M_w 4.1) of the Guthrie sequence that occurred about ten months following fault activation. The sequence shows overall temporal correlation with the injection rate of nearby wells, showing that it is largely driven by injection (Chen et al., 2018; Haffener et al., 2018). The subevent modeling by Wu et al. (2019) of the M_w 4.1 indicates a complex failure that contains 5 subevents, which indicates a complex triggering and rupture process. In this study, we model the spatial and temporal evolution of the M_w 4.1 earthquake rupture and its relationship with prior seismicity to better understand the nucleation and triggering of large events during induced earthquake sequences. We quantify the distribution of asperities based on spatial gridding analysis and compare with other M4-5 earthquakes in both induced intraplate and interplate earthquake sequences, to better constrain the control factors of earthquake rupture complexity from different tectonic environments.

2 Data:

The sequence is comprised of 936 events which were analyzed in detail and relocated by (Chen et al., 2018; Chen & Abercrombie, 2020). The sequence started in early 2014 and intensifies in July 2014 following an injection rate increase from nearby disposal wells, and gradually decreases in activity following the shut-in of nearby wells in May 2015. A majority of the sequence occurred on two parallel 4 km long SE tending faults, which is bisected by an orthogonal fault trending to the NE (Benz et al., 2015; Chen et al., 2018) (Figure 1a). The M_w 4.1 occurred on April 8, 2015 at 16:51:13 (UTC) along the main fault trending to SE, 10 months after seismicity began on that fault.

Due to the small magnitude of the target event, empirical Green's function (EGF) method is used to retrieve source properties (Hartzell, 1978). The EGF event chosen is a nearly co-located M3.1 earthquake that occurred on September 15, 2014 at 00:10:38 (UTC), which has similar focal mechanism with the target event and was previously used in the time-domain deconvolution of Wu et al. (2019). We download waveform data from Incorporated Research Institutes of Seismology (IRIS) data management center for 23 stations within 75 km of the target event and manually pick both P and S phases. Data utilized in the inversion are required to have: >2s S-P travel time, an impulsive first motion, $\geq$ 100 Hz sampling rate, and a signal to noise ratio $\geq$ 10. 11 out of the original 23 stations pass these criteria and are utilized in the inversion (Figure 1c).

Only the P-wave is used for the finite slip inversion analysis of the target earthquake. This is based on the results from Wu et al. (2019) that the small initial sub-event is masked in the S-wave arrival by the P-wave's coda. The waveforms for the target and

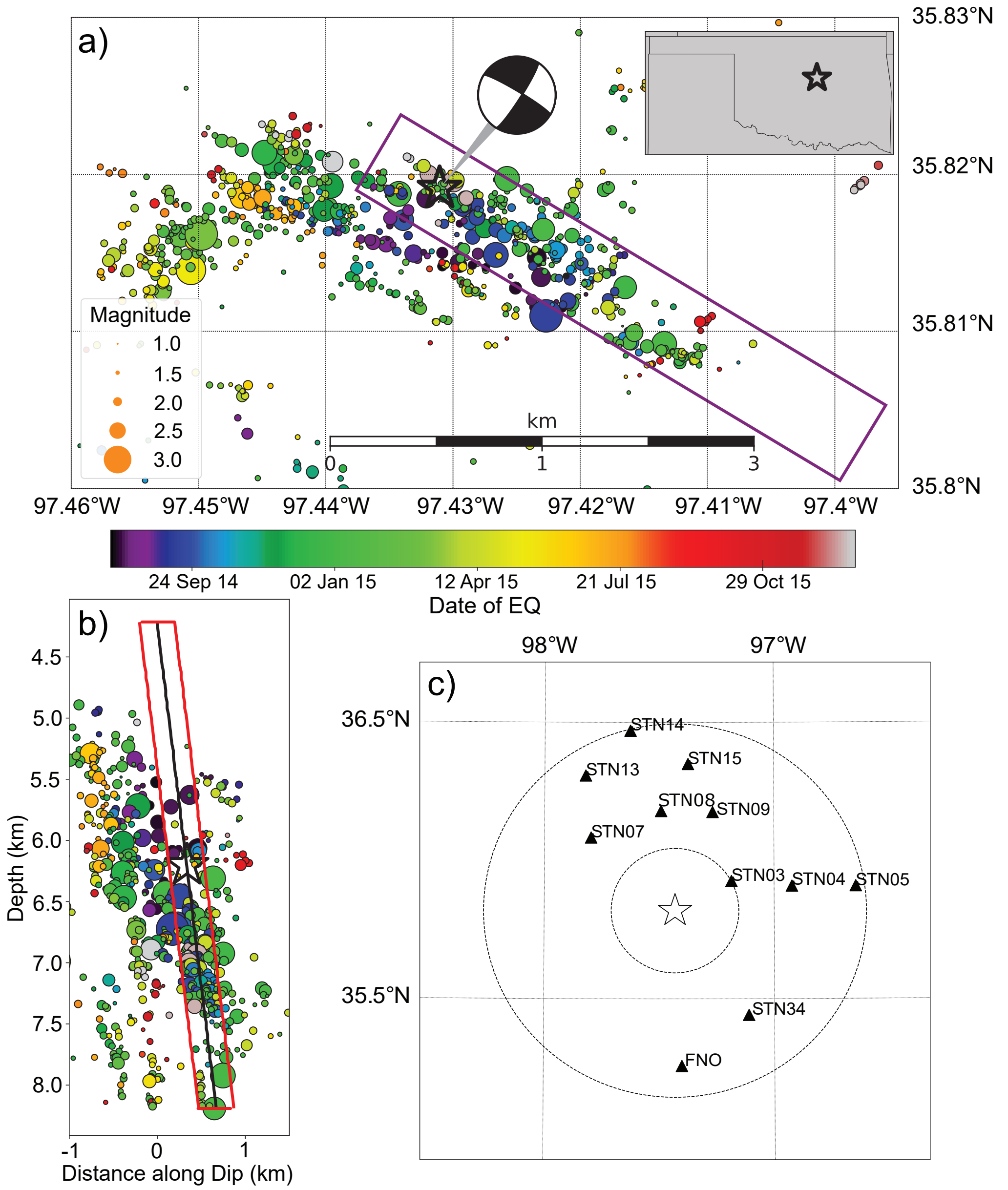

Figure 1. a) Map view of the Guthrie earthquake sequence with earthquakes colored by date and scaled by magnitude. The M_w 4.1 (black star) and model fault (purple box) are also shown. (b) Perpendicular cross section across modeled model fault. Model fault is shown as black line, red box denote distance of 200m from model fault. Earthquakes that fall within these red bars are plotted on modeled slip in Figure 3. (c) Map view of stations (black triangles) used in the inversion, circles mark 25 km and 75km distance interval from event epicenter location (black star)

the EGF earthquakes are integrated to displacement, band-pass-filtered between 1 and 10 Hz, resampled to 100 Hz, and normalized by the maximum absolute value of the target earthquake for each component. The data was cut 0.5 seconds before the P arrival and 2.5 seconds after, with the exception of STN03 which was closer in distance to the target event and was cut to 2.2 seconds. The channels utilized in the inversion process are the vertical component and the horizontal channel with highest amplitude. Due to the horizontal channels having lower signal to noise, they are given half of the weight of the vertical components in the inversion.

3 Method:

To constrain the slip of the M_w 4.1 earthquake, we apply a linear slip inversion method (Hartzell & Heaton, 1986; Uchide & Ide, 2007) based on empirical Green's Function (EGF) (Hartzell, 1978). The workflow from Uchide and Song (2018) is followed to perform the inversion:

1. The creation of the fault model over which the spatio-temporal slip distribution will be calculated. We estimate the fault orientation using the target earthquakes focal mechanism and the distribution of aftershocks and find a strike, dip and rake of 301° , 81° , and -10° respectively, which agrees the directivity estimate of 126.3° (Wu et al., 2019). We base the extent of the fault model on the locations of the sub-events found in the modeling by Wu et al. (2019), and refine it through trial and error. The final fault model is 4 km long (along strike) and 4 km wide (along dip), and the earthquake hypocenter is located 0.5 km along strike and 2 km along dip (Figure 2a).
2. A linear cubic B-spline function is chosen as the basis function to describe the spatiotemporal slip-distribution. The basis function has spatial nodes along the fault at intervals of 0.25 km and at 0.1 s intervals in time. The expansion coefficients controlling the amplitude of the basis function are the unknown parameters and will estimated during the inversion. To reduce the number of parameters that are being solved for, the start time of the first temporal basis function at each grid point is set to a time when the rupture reaches that point and is restricted to 0.5 s in length. This assumes a causality between the rupture front and onset of slip and introduces the unknown parameter of hypothetical rupture velocity V_{hr}.

3. The determination of a hypothetical rupture velocity V_{hr}. The V_{hr} controls when the rupture arrives at a grid point and therefore should be faster than the true rupture velocity. In order to determine the optimal V_{hr} we perform the inversion with multiple velocities from 1.6 km/s to 4.4 km/s at an interval of 0.2 km/s. The model performance is measured by the variance reduction observed between the synthetic and observed waveforms defined as $1-\frac{Var(d_{obs}-d_{syn})}{Var(d_{obs})}$, where Var is variance and d_{syn} and d_{obs} are the synthetic observed waveforms.
4. In the final step we solve for the unknown expansion coefficients controlling the amplitude of the basis function using a non-negative least squares algorithm (Lawson & Hanson, 1987). In order to reduce the difference between the coefficients of spatio-temporally neighboring basis functions and aid in the convergence toward a solution, we introduce a temporal smoothing constraint. This assumes that the rupture process progresses in a relatively smooth manner. We consider the intensity of this constraint as a hyperparameter in Bayesian modeling and find through the minimization of Akaike's Bayesian information criterion (Akaike, 1980; Ide, 2001; Uchide & Ide, 2007; Uchide & Song, 2018; Yabuki & Matsu'ura, 1992).

4 Results:

Figure 2 depicts the results for the M_w 4.1 earthquake. The estimated model produces good agreement between observed and synthetic waveforms with a variance reduction of 73.9%. This result was obtained using a V_{hr} of 3.2 km/s, which is the velocity where improvement in variance reduction is < 0.01. This value agrees falls within the range of 3.0 km/s and 3.5 km/s found in other studies using the same method (Uchide & Song, 2018), but is higher than the 1.6 - 1.8 km/s found for this event by Wu et al. (2019).

The resolved moment is 3.25×10^{15} Nm, which is equivalent to a M_w 4.3. The seismic moment and amount of fault slip are estimated as relative values to the EGF event's moment and would decrease if it had a lower magnitude. To test the robustness of the moment, alternative M2.1 EGF was tested, which produced a similar seismic moment and slip distribution but had lower variance reduction.

The source time function shown in Figure 2c has a total duration of 1.1 seconds and 3 distinct moment rate pulses. Figure 2d shows detailed spatiotemporal evolution

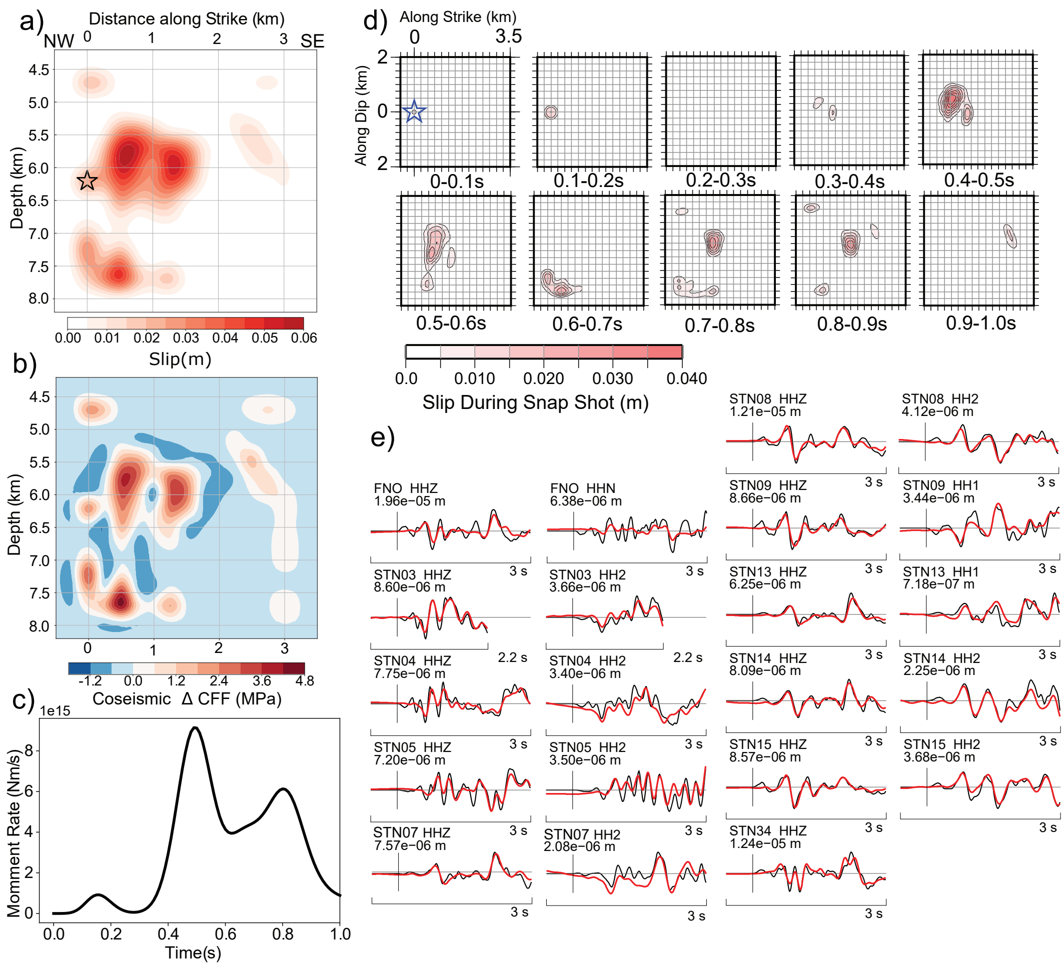

Figure 2. Slip inversion analysis results for the mainshock. (a) distribution of the final slip. (b) Distribution of the stress change. (c). Moment rate function. (d) Snapshots of the distribution of the slip rate as specified time intervals. (e) Comparison of between the observed (black) and synthetic waveforms (red).

of the rupture process: (1) rupture initiated around the hypocenter with the first small pulse; (2) after a gap of 0.1 s, the 2nd larger slip patch starts with 250 m SE of the first, which gradually propagate along strike; (3) at about 0.5 s, rupture propagates to a 3rd slip patch at deeper depth; (4) at about 0.7 s, a 4th slip patch adjacent to the 2nd patch is activated. The along-strike locations of these slip patches closely align with the previous sub-event modeling done by Wu et al. (2019), with the exception of one of the slip patches in our model occurring at a deeper depth.

Based on the estimated slip model, the stress drop distribution is calculated using the code from Okada et al. (2000) (Figure 2b). Maximum stress drop of 4.6 MPa occurred during the 3rd slip patch at deeper depth. The 1st, 2nd, and 4th slip patches experienced peak stress drops of 1.8, 4.2, 3.2 MPa, respectively. The average stress drop from grids with stress drop above 0.5 MPa is 1.6 MPa, which is lower than the values of 3.4 to 3.9 MPa obtained by other studies (Wu et al., 2019; Chen & Abercrombie, 2020). The slip model's stress drop values are highly dependent on the spatial resolution of the grid, so the values of peak stress drop should be considered the lower bound of actual values.

5 Discussion:

5.1 The Role of Prior Seismicity and Injection on Rupture Propagation.

It has been observed in other swarms that the slip of prior seismicity often outlines the slip of future events (Ide, 2002). To investigate the relationship between cumulative slip from prior seismicity and the largest event, we first estimate the rupture radius of earlier earthquakes based on the equation: $r = (0.32\beta)/f_c$ (Eshelby, 1957; Madariaga, 1976), where f_c is the corner frequency, and β is 3.35 km/s, which is the average S-wave velocity between 1.5 and 8 km depth. This assumes a simple circular rupture, which may differ from actual rupture area. Then, we calculate cumulative stress drop within the fault zone for each location by adding stress drops from events with overlapping rupture areas. The corner frequency (f_c) and stress drop ($\Delta\sigma$) values for each event are obtained from S-wave spectral analysis in Chen and Abercrombie (2020). The results of this analysis are plotted in Figure 3. The key observations include:

1. Slip from previous earthquakes primarily concentrates within the gap between the deeper and shallower slip patches (Figure 3). The abundance of seismicity and stress

release in that region likely inhibited significant amount of slip during the largest event. The accumulated stress changes from these smaller events at deeper depth may have promoted activation of the 3rd slip patch during the largest event (M. Brown & Ge, 2018).

2. Those events that do overlap with the slip model are among the earliest earthquakes to occur and have relatively lower stress drop, coinciding with the low stress drop area between the 2nd and 4th slip patches during the largest earthquake (Figure 3a). This is similar to findings for other swarms where stress drops are often lower for overlapping events that occur after previous earthquakes (Ide, 2002).
3. These observations suggest that slip from early events can influence the slip distribution of a later larger event, suggesting importance of earthquakes themselves in sequence evolution and rupture propagation. The median relative location errors from Chen et al. (2018) is estimated to be 10m horizontally and 20m vertically with over 90% of events having location errors within 100m. Although the absolute locations can be systematically shifted, the relatively spatial patterns shown in Figure 3 should be robust.

Without detailed pore pressure change modeling along the fault's surface, which is beyond the scope of this paper, it is not possible to isolate the effects of pore pressure on slip distribution of an earthquake. Certain attributes of finite slip model can be linked to pore pressure changes based on past studies that performed modeling (Galis et al., 2017; Norbeck & Horne, 2016) and rupture directivity analysis (Lui & Huang, 2019; Folesky et al., 2016). These studies show that in general, rupture tends to propagate away from the area of injection when the absolute pore pressure perturbation is relatively low. When pore pressure perturbations are high, the rupture tends to propagate towards the injection area, for example, the 2016 M_w 5.1 Fairview earthquake propagated towards high-rate injection zones (Lui & Huang, 2019).

Due to the relatively low injection volume from nearby disposal wells (within 5 km), the cumulative pore pressure within the Guthrie fault is only about 0.003 MPa, much lower than pressure modeling from other regions (Chen et al., 2018). Despite the relatively low-pressure amplitude, the diffusive migration of seismicity away from earliest seismicity suggest pressure diffusion within the fault zone (Figure 3a). Therefore, the first sub-event is likely initiated due to accumulated pore pressure. The rupture propagation

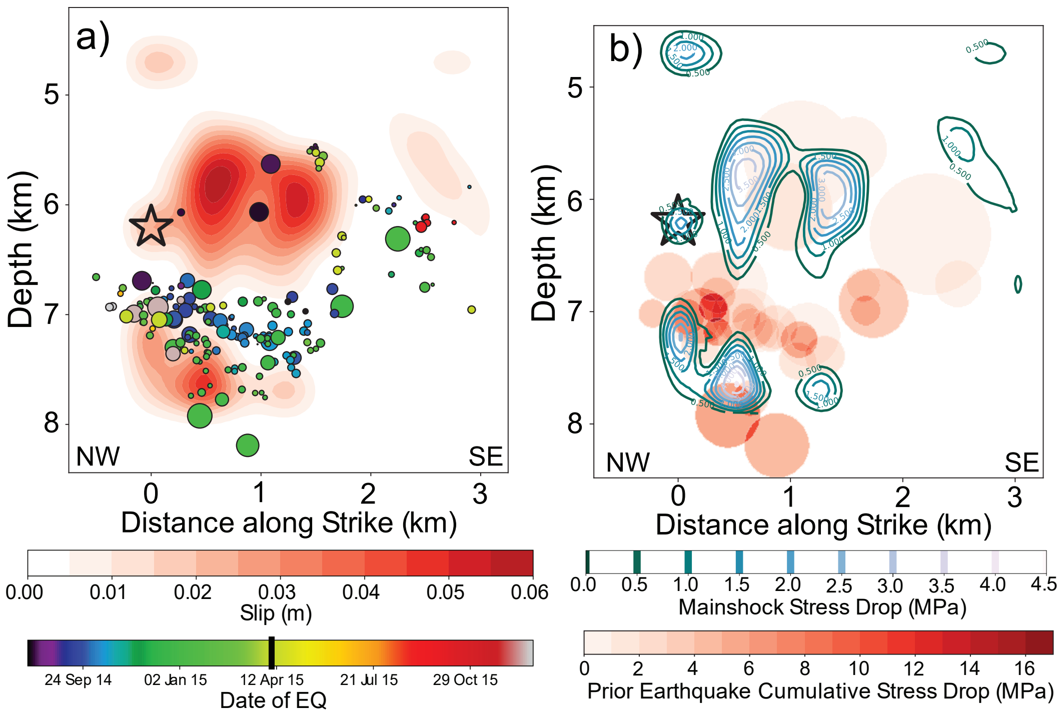

Figure 3. (a) Distribution of the final slip with mainshocks hypocenter (black star) and earthquakes within 200m of modeled fault shown. Earthquakes are scaled by magnitude and colored by date.(b) Stress drop distribution of modeled earthquake (blue contours). Cumulative stress drop along the model fault caused by previous seismicity (red shaded region).

away from possibly dominating disposal well is consistent with the mechanical model proposed in Galis et al. (2017).

5.2 Rupture Complexity

The well separated slip patches of the Guthrie M_w4.1 earthquake resembles the finite rupture model of the 2011 Prague and one of the models of 2016 Pawnee earthquake (Sun & Hartzell, 2014; Grandin et al., 2017). These events all exhibit complex cascading ruptures where multiple separated slip patches combine to produce a large magnitude earthquake (Ellsworth & Beroza, 1995). Rupture complexity for global large magnitude earthquakes shows spatial coherency and correlation with local geological structures (Ye et al., 2018). While we observe the influence of prior seismicity on the slip distributions of the Guthrie earthquake, this is not well observed for the Prague and Pawnee earthquakes. We hypothesize that the complex slip patterns of Oklahoma induced earthquakes may likely be due to higher fault zone heterogeneity of intraplate faults with low tectonic loading rates .

To test this hypothesis, we compare the slip complexity observed in events in Oklahoma with other similar sized earthquakes from other tectonic environments, ideally strike-slip earthquakes that occur in swarm-like sequences. The events from tectonically active regions that we compare to are 7 earthquakes from 1998 Hida-Mountains Swarm sequence in Japan (Ide, 2001) and the two largest events that occurred in the 2012 Brawley swarm in Imperial Valley, California (Wei et al., 2013). These events are chosen because they occur in swarm-like sequences that were driven by static stress changes and induced or natural pore pressure change (Aoyama, 2002; Wei et al., 2015). We obtain slip models for the 9 earthquakes, which have a magnitude range of 4.1 - 5.4 from the finite fault database SRCMOD (Mai & Thingbaijam, 2014). We compared these events to the Guthrie M_w 4.1 and the Prague M_w 5.6 (Sun & Hartzell, 2014) slip models, but not the Pawnee M_w5.6 because it has multiple conflicting slip models (Grandin et al., 2017; Moschetti et al., 2019).

In order to quantify the number and the characteristics of the slip patches that occur in each model, we follow a similar approach to Somerville et al. (1999). First, we trim the model to contain only the region where a majority of slip occurred by removing the edges of the finite fault model that have a mean slip less than half the entire model's mean slip. Next, we isolate the grid points that have slip values greater than or equal to the 80 percentiles of the slip distribution of the trimmed fault. We then group these grid points using the method of Haralick and Shapiro (1992) and a criterion of 4-way connectivity, which means that if grid points are connected either vertically or horizontally, they are grouped together. Of the final groups we remove those with fewer than 2 grid points.

The number of slip patches observed for each earthquake can be found in supplemental Table S1 and their individual plots in supplemental Figure S1. In each region, the average number of slip patches observed per earthquake is roughly 7, 2, 2 for Oklahoma, Brawley Swarm and the Hida-Mountain Swarm, respectively. For each slip patch we calculate its area as a fraction of the total area of the trimmed model (normalized area), and its slip as a fraction of the average slip over the trimmed fault (normalized slip). In Oklahoma, the normalized area of the slip patches is significantly smaller than what is observed in Hida and Brawley (Figure 4b). The normalized slip of the slip patches is highest for Oklahoma (2 to 3), while relatively smaller for Brawley (1.5 to 2.5) and Hida (1 to 2) (Figure4a). This suggests that the slip for Hida and Brawley earthquakes is more diffuse and covers more of the rupture area. In contrast, Oklahoma earthquakes tend to have slip concentrated in small or isolated patches. These differences between induced intraplate earthquakes in Oklahoma and induced/natural earthquakes at plate boundaries suggest that the dormant faults in intraplate regions might exhibit different behavior from plate boundary regions, and ruptures in intraplate regions may be more complex than similar magnitude interplate events. We should note that the sample size is relatively small due to limited slip models for M4-5 strike-slip earthquakes and resolution of the models differs between studies, the latter of which could limit the number of isolated slip patches (L. Brown et al., 2015). Future studies of more systematic comparisons can further address this hypothesis.

6 Conclusion:

The finite slip inversion indicates that moderate sized earthquakes in Oklahoma have complex ruptures with multiple slip patches. Our analyses find the following:

- The Guthrie earthquake, high slip patches are surrounded by prior seismicity, indicating that the slip patches likely represent relatively stronger asperities.

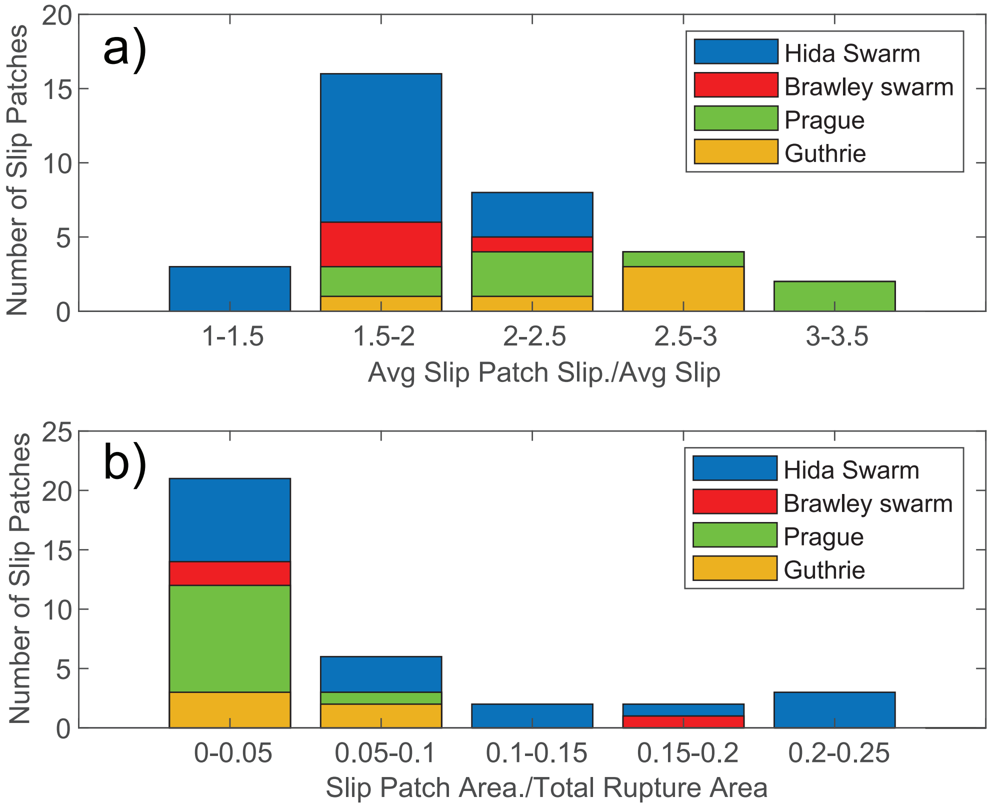

Figure 4. Histogram of the normalized slip (a) and normalized area (b) for the asperities observed in each region. Note that Prague and Guthrie have higher concentrations of slip in within asperities (a) and they also have smaller asperities (b).

- Both of the two Oklahoma earthquakes analyzed here exhibit higher levels of slip heterogeneity compared to other regions.
- The heterogeneity of slip observed in Oklahoma can be attributed to both fault characteristics, prior seismicity, and to injection.

We find that both pore pressure perturbations, earthquake interactions, and fault characteristics control rupture propagation in moderate size earthquakes in Oklahoma. In order to properly understand the potential magnitude ranges we could expect from a fault a full understanding of that fault's geometry and characteristics is required.

Acknowledgments

This work is partially supported by NSF award 1547071, and a graduate student scholarship from the University of Oklahoma. The waveform data used in this study were obtained from the IRIS Data Management Center (https://ds.iris.edu/ds/nodes/dmc/). The finite fault slip inversions of the Hida and Brawley earthquakes are downloaded from the SRCMOD Earthquake Finite Fault Database (Mai & Thingbaijam, 2014). The Prague earthquakes finite fault model was obtained directly from Sun and Hartzell (2014). The datasets for relocated catalog and stress drop estimates are available from Chen et al. (2018) and Chen and Abercrombie (2020).

References

Akaike, H. (1980, 2). Likelihood and the Bayes procedure. In J. Bernardo, M. De Groot, D. Lindley, & A. Smith (Eds.), *Bayesian statistics* (pp. 143–166). Calencia, Spain: University Press.

Aoyama, H. (2002). Evolution mechanisms of an earthquake swarm under the Hida Mountains, central Japan, in 1998. *Journal of Geophysical Research*, *107*(B8). doi: 10.1029/2001jb000540

Benz, H. M., Mcmahon, N. D., Aster, R. C., McNamara, D. E., & Harris, D. B. (2015). Hundreds of Earthquakes per Day: The 2014 Guthrie, Oklahoma, Earthquake Sequence. *Seismological Research Letters*, *86*(5), 1318–1325. doi: 10.1785/0220150019

Brown, L., Wang, K., & Sun, T. (2015). Static stress drop in the Mw 9 Tohoku-oki earthquake: Heterogeneous distribution and low average value. *Geophysical Research Letters*, *42*(24), 10595–10600. doi: 10.1002/2015GL066361

Brown, M., & Ge, S. (2018, 6). Small Earthquakes Matter in Injection-Induced Seismicity. *Geophysical Research Letters*, *45*(11), 5445–5453. doi: 10.1029/2018GL077472

Chen, X., & Abercrombie, R. E. (2020, 6). Improved approach for stress drop estimation and its application to an induced earthquake sequence in Oklahoma. *Geophysical Journal International*. doi: 10.1093/gji/ggaa316

Chen, X., Haffener, J., Goebel, T. H., Meng, X., Peng, Z., & Chang, J. C. (2018). Temporal Correlation Between Seismic Moment and Injection Volume for an Induced Earthquake Sequence in Central Oklahoma. *Journal of Geophysical Research: Solid Earth*. doi: 10.1002/2017JB014694

Chen, X., Nakata, N., Pennington, C., Haffener, J., Chang, J. C., He, X., ... Walter, J. I. (2017, 12). The Pawnee earthquake as a result of the interplay among injection, faults and foreshocks. *Scientific Reports*, *7*(1), 4945. doi: 10.1038/s41598-017-04992-z

Ellsworth, W. L. (2013, 7). Injection-Induced Earthquakes. *Science*, *341*(6142), 1225942–1225942. doi: 10.1126/science.1225942

Ellsworth, W. L., & Beroza, G. C. (1995, 5). Seismic Evidence for an Earthquake Nucleation Phase. *Science*, *268*(5212), 851–855. doi: 10.1126/science.268.5212.851

Eshelby, J. D. (1957). The determination of the elastic field of an ellipsoidal inclusion, and related problems. *Proc. R. Soc. London, Ser. A,*, *241*, 376–396.

Folesky, J., Kummerow, J., Shapiro, S. A., Häring, M., & Asanuma, H. (2016). Rupture directivity of fluid-induced microseismic events: Observations from an enhanced geothermal system. *Journal of Geophysical Research: Solid Earth*, *121*(11), 8034–8047. doi: 10.1002/2016JB013078

Galis, M., Ampuero, J. P., Mai, P. M., & Cappa, F. (2017). Induced seismicity provides insight into why earthquake ruptures stop. *Science Advances*. doi: 10.1126/sciadv.aap7528

Grandin, R., Vallée, M., & Lacassin, R. (2017, 7). Rupture Process of the M w 5.8 Pawnee, Oklahoma, Earthquake from Sentinel-1 InSAR and Seismological Data. *Seismological Research Letters*, *88*(4), 994–1004. doi: 10.1785/0220160226

Haffener, J., Chen, X., & Murray, K. (2018, 9). Multi-scale analysis of spatiotemporal relationship between injection and seismicity in Oklahoma. *Journal of Geophysical Research: Solid Earth*. doi: 10.1029/2018JB015512

Haralick, R. M., & Shapiro, L. G. (1992). *Computer and Robot Vision* (1st ed.). USA: Addison-Wesley Longman Publishing Co., Inc.

Hartzell, S. (1978, 1). Earthquake aftershocks as Green's functions. *Geophysical Research Letters*, *5*(1), 1–4. doi: 10.1029/GL005i001p00001

Hartzell, S., & Heaton, T. (1986). Rupture history of the 1984 Morgan Hill, California, earthquake from the inversion of strong motion records. *Bulletin of the Seismological Society of America*.

Hartzell, S., Mendoza, C., & Zeng, Y. (2013). Rupture model of the 2011 Mineral, Virginia, earthquake from teleseismic and regional waveforms. *Geophysical Research Letters*, *40*(21), 5665–5670. doi: 10.1002/2013GL057880

Ide, S. (2001). Complex source processes and the interaction of moderate earthquakes during the earthquake swarm in the Hida-Mountains, Japan, 1998. *Tectonophysics*, *334*(1), 35–54. doi: 10.1016/S0040-1951(01)00027-0

Ide, S. (2002). Estimation of radiated energy of finite-source earthquake modeling. *Bull. Seismol. Soc. Am.*, *92*(8), 2994–3005.

Keranen, K. M., Weingarten, M., Abers, G. A., Bekins, B. A., & Ge, S. (2014, 7). Sharp increase in central Oklahoma seismicity since 2008 induced by massive wastewater injection. *Science*, *345*(6195), 448–451. doi: 10.1126/science.1255802

Lawson, C. L., & Hanson, R. J. (1987). *Solving Least Squares Problems (Classics in Applied Mathematics)*. doi: 10.1137/1.9781611971217

Lui, S. K. Y., & Huang, Y. (2019). Do Injection-Induced Earthquakes Rupture Away from Injection Wells due to Fluid Pressure Change? *Bulletin of the Seismological Society of America*, *109*(1), 358–371. doi: 10.1785/0120180233

Madariaga, R. (1976). Dynamics of an expanding circular fault. *Bull. Seismol. Soc. Am.*, *66*(3), 639–666.

Mai, P. M., & Thingbaijam, K. K. S. (2014). SRCMOD: An Online Database of Finite-Fault Rupture Models. *Seismological Research Letters*, *85*(6), 1348–1357. doi: 10.1785/0220140077

Moschetti, M. P., Hartzell, S. H., & Herrmann, R. B. (2019, 3). Rupture Model of the M5.8 Pawnee, Oklahoma, Earthquake From Regional and Teleseismic Waveforms. *Geophysical Research Letters*, *46*(5), 2494–2502. doi: 10.1029/2018GL081364

Norbeck, J. H., & Horne, R. N. (2016, 12). Evidence for a transient hydromechanical and frictional faulting response during the 2011 M w 5.6 Prague, Oklahoma earthquake sequence. *Journal of Geophysical Research: Solid Earth*, *121*(12), 8688–8705. doi: 10.1002/2016JB013148

Okada, Y., Yamamoto, E., & Ohkubo, T. (2000). Coswarm and preswarm crustal deformation in the eastern Izu Peninsula, Centeral Japan. *J. Geophys. Res.*, *105*(1), 681–692.

Pennington, C., & Chen, X. (2017, 7). Coulomb Stress Interactions during the M w 5.8 Pawnee Sequence. *Seismological Research Letters*, *88*(4), 1024–1031. doi: 10.1785/0220170011

Qin, Y., Chen, X., Carpenter, B. M., & Kolawole, F. (2018). Coulomb Stress Transfer Influences Fault Reactivation in Areas of Wastewater Injection. *Geophysical Research Letters*. doi: 10.1029/2018GL079713

Somerville, P., Irikura, K., Graves, R., Sawada, S., Wald, D., Abrahamson, N., ... Kowada, A. (1999). Characterizing crustal earthquake slip models for the prediction of strong ground motion. *Seismological Research Letters*, *70*(1), 59–80. doi: 10.1785/gssrl.70.1.59

Sumy, D. F., Cochran, E. S., Keranen, K. M., Wei, M., & Abers, G. A. (2014, 3). Observations of static Coulomb stress triggering of the November 2011 M 5.7 Oklahoma earthquake sequence. *Journal of Geophysical Research: Solid Earth*, *119*(3), 1904–1923. doi: 10.1002/2013JB010612

Sun, X., & Hartzell, S. (2014). Finite-fault slip model of the 2011 Mw 5.6 Prague, Oklahoma earthquake from regional waveforms. *Geophysical Research Letters*, *41*(12), 4207–4213. doi: 10.1002/2014GL060410

Uchide, T., & Ide, S. (2007). Development of multiscale slip inversion method and its application to the 2004 mid-Niigata Prefecture earthquake. *Journal of Geophysical Research: Solid Earth*, *112*(6), 1–20. doi: 10.1029/2006JB004528

Uchide, T., & Song, S. G. (2018). Fault Rupture Model of the 2016 Gyeongju, South Korea, Earthquake and Its Implication for the Underground Fault System. *Geophysical Research Letters*, *45*(5), 2257–2264. doi: 10.1002/2017GL076960

Wei, S., Avouac, J. P., Hudnut, K. W., Donnellan, A., Parker, J. W., Graves, R. W.,

... Eneva, M. (2015). The 2012 Brawley swarm triggered by injection-induced aseismic slip. *Earth and Planetary Science Letters*, *422*, 115–125. doi: 10.1016/j.epsl.2015.03.054

Wei, S., Helmberger, D., Owen, S., Graves, R. W., Hudnut, K. W., & Fielding, E. J. (2013). Complementary slip distributions of the largest earthquakes in the 2012 Brawley swarm, Imperial Valley, California. *Geophysical Research Letters*, *40*(5), 847–852. doi: 10.1002/grl.50259

Wu, Q., Chen, X., & Abercrombie, R. E. (2019). Source Complexity of the 2015 Mw 4.0 Guthrie, Oklahoma Earthquake. *Geophysical Research Letters*, *46*(9), 4674–4684. doi: 10.1029/2019GL082690

Yabuki, T., & Matsu'ura, M. (1992). Geodetic data inversion using a Bayesian information criterion for spatial distribution of fault slip. *Geophysical Journal International*. doi: 10.1111/j.1365-246X.1992.tb00102.x

Ye, L., Kanamori, H., & Lay, T. (2018). Global variations of large megathrust earthquake rupture characteristics. *Science Advances*, *4*(3), 1–8. doi: 10.1126/sciadv.aao4915

Figure1_Mapview.

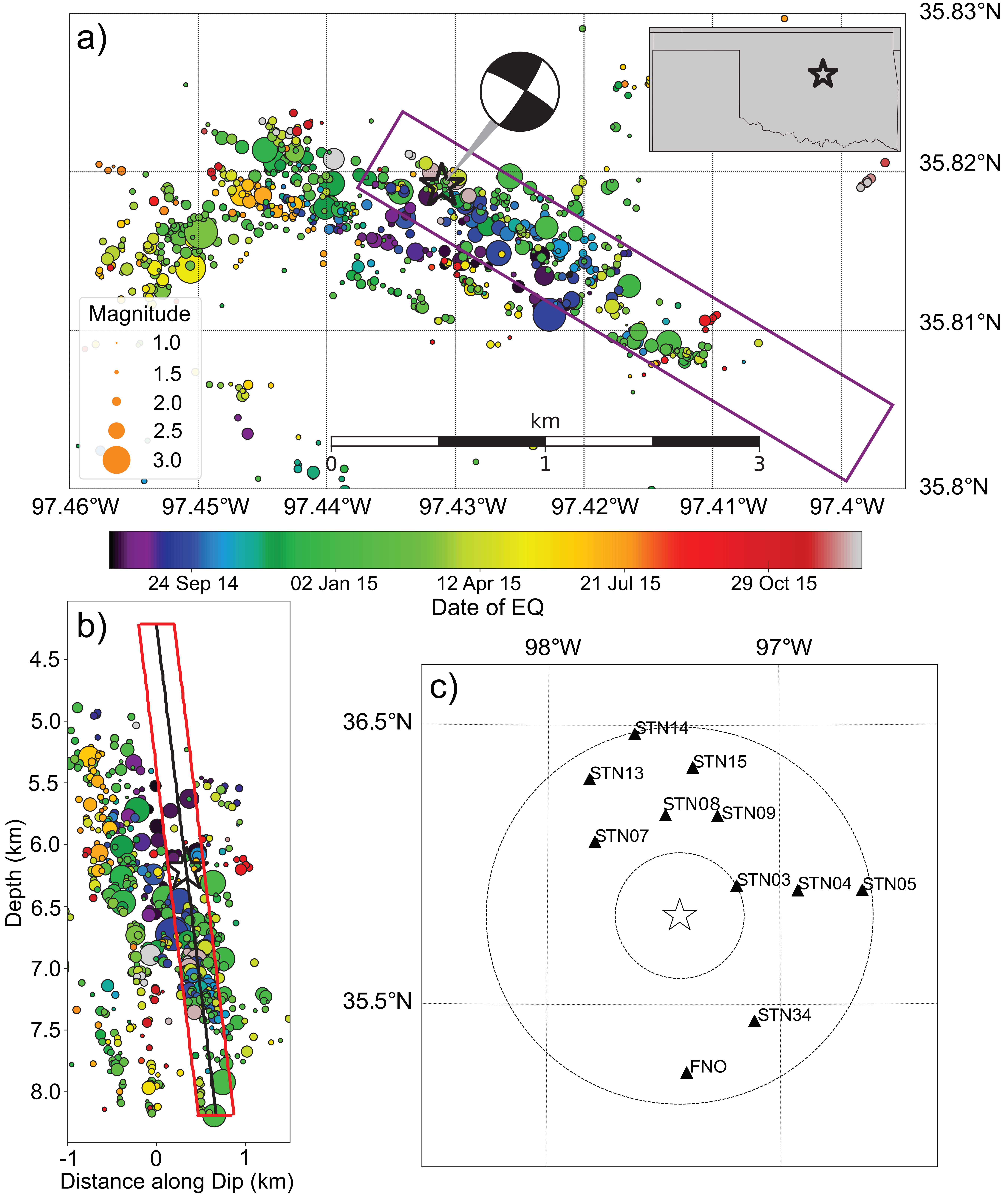

a)
35.83°N
35.82°N
35.81°N
35.8°N
97.46°W
97.45°W
97.44°W
97.43°W
97.42°W
97.41°W
97.4°W
Magnitude
1.0
1.5
2.0
2.5
3.0
km
0
1
3
24 Sep 14
02 Jan 15
12 Apr 15
21 Jul 15
29 Oct 15
Date of EQ
b)
Depth (km)
4.5
5.0
5.5
6.0
6.5
7.0
7.5
8.0
-1
0
1
Distance along Dip (km)
c)
98°W
97°W
36.5°N
35.5°N
STN14
STN15
STN13
STN08
STN09
STN07
STN03
STN04
STN05
STN34
FNO

Figure2_inversion.

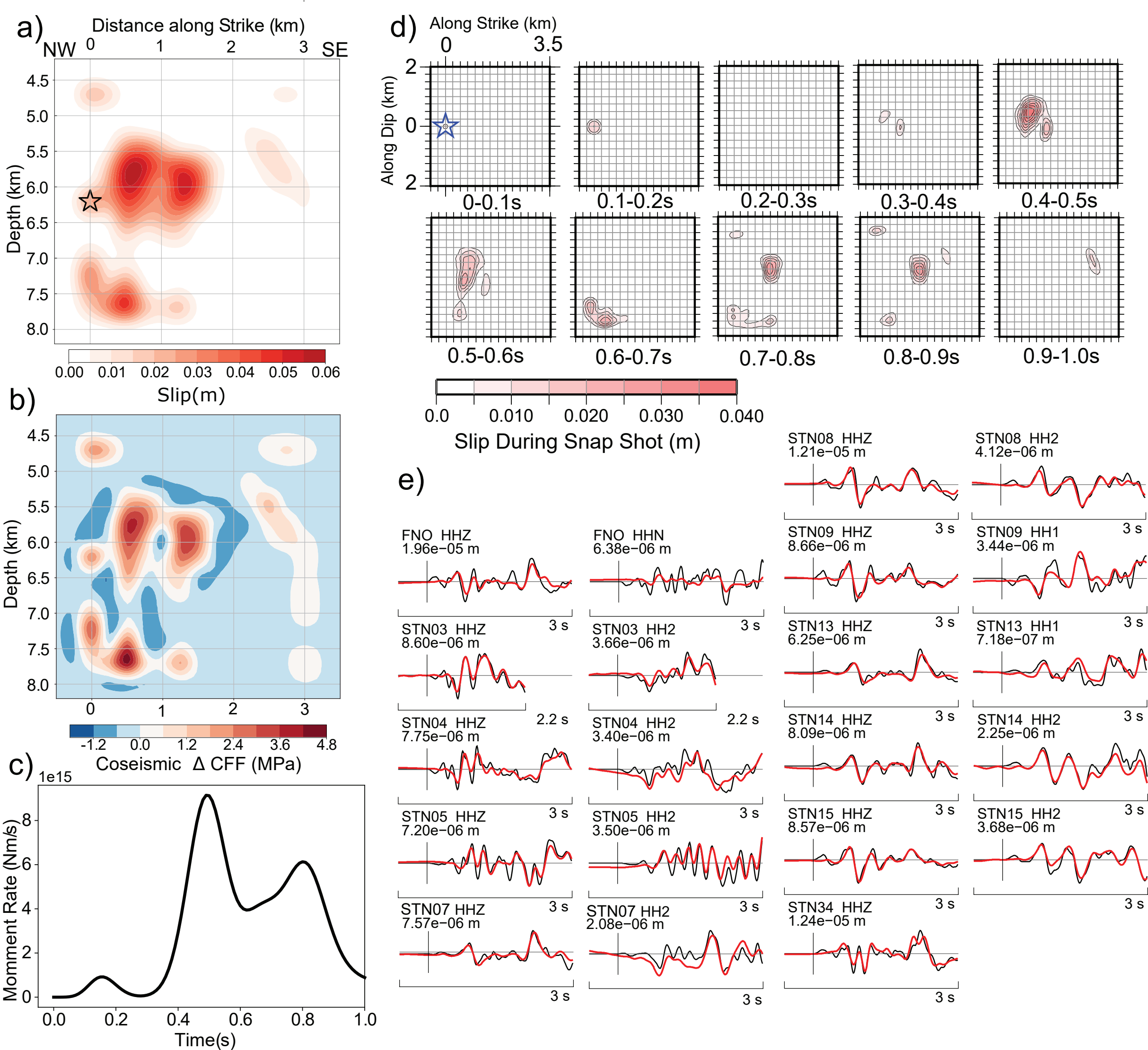

a)
Distance along Strike (km)
NW
SE
0
1
2
3
Depth (km)
4.5
5.0
5.5
6.0
6.5
7.0
7.5
8.0
0.00
0.01
0.02
0.03
0.04
0.05
0.06
Slip(m)
b)
Depth (km)
-1.2
0.0
1.2
2.4
3.6
4.8
Coseismic Δ CFF (MPa)
c)
1e15
Momment Rate (Nm/s)
0
2
4
6
8
0.0
0.2
0.4
0.6
0.8
1.0
Time(s)
d)
Along Strike (km)
0
3.5
Along Dip (km)
2
0
2
0-0.1s
0.1-0.2s
0.2-0.3s
0.3-0.4s
0.4-0.5s
0.5-0.6s
0.6-0.7s
0.7-0.8s
0.8-0.9s
0.9-1.0s
0.0
0.010
0.020
0.030
0.040
Slip During Snap Shot (m)
e)
FNO HHZ 1.96e−05 m
FNO HHN 6.38e−06 m
STN03 HHZ 8.60e−06 m
STN03 HH2 3.66e−06 m
STN04 HHZ 7.75e−06 m
STN04 HH2 3.40e−06 m
STN05 HHZ 7.20e−06 m
STN05 HH2 3.50e−06 m
STN07 HHZ 7.57e−06 m
STN07 HH2 2.08e−06 m
STN08 HHZ 1.21e−05 m
STN08 HH2 4.12e−06 m
STN09 HHZ 8.66e−06 m
STN09 HH1 3.44e−06 m
STN13 HHZ 6.25e−06 m
STN13 HH1 7.18e−07 m
STN14 HHZ 8.09e−06 m
STN14 HH2 2.25e−06 m
STN15 HHZ 8.57e−06 m
STN15 HH2 3.68e−06 m
STN34 HHZ 1.24e−05 m
3 s
2.2 s

Figure3_Prior_slip.

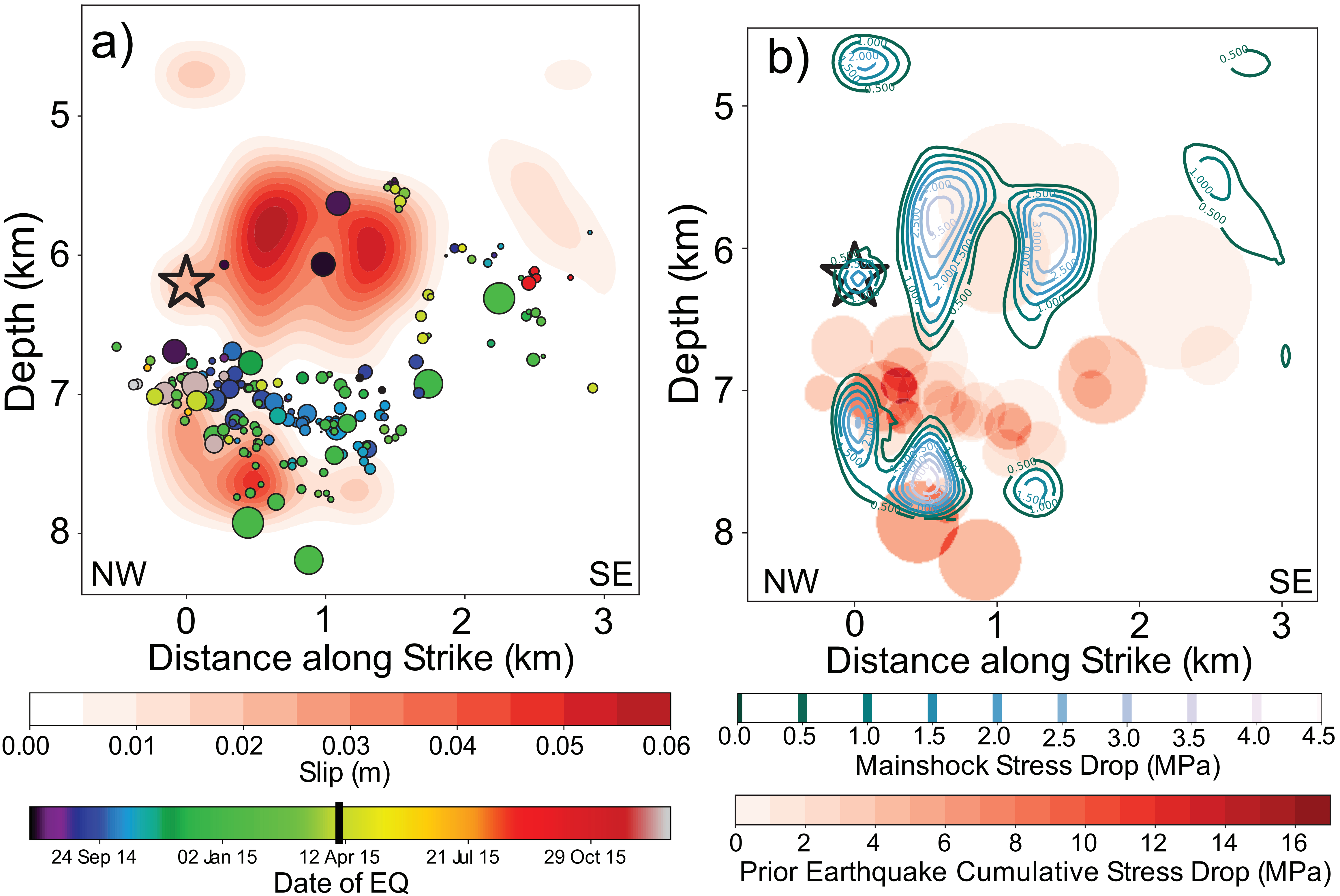

a)
Depth (km)
5
6
7
8
NW
SE
0
1
2
3
Distance along Strike (km)
b)
Depth (km)
5
6
7
8
NW
SE
0
1
2
3
Distance along Strike (km)
0.00
0.01
0.02
0.03
0.04
0.05
0.06
Slip (m)
24 Sep 14
02 Jan 15
12 Apr 15
21 Jul 15
29 Oct 15
Date of EQ
0.0
0.5
1.0
1.5
2.0
2.5
3.0
3.5
4.0
4.5
Mainshock Stress Drop (MPa)
0
2
4
6
8
10
12
14
16
Prior Earthquake Cumulative Stress Drop (MPa)

Figure4_other_regions.

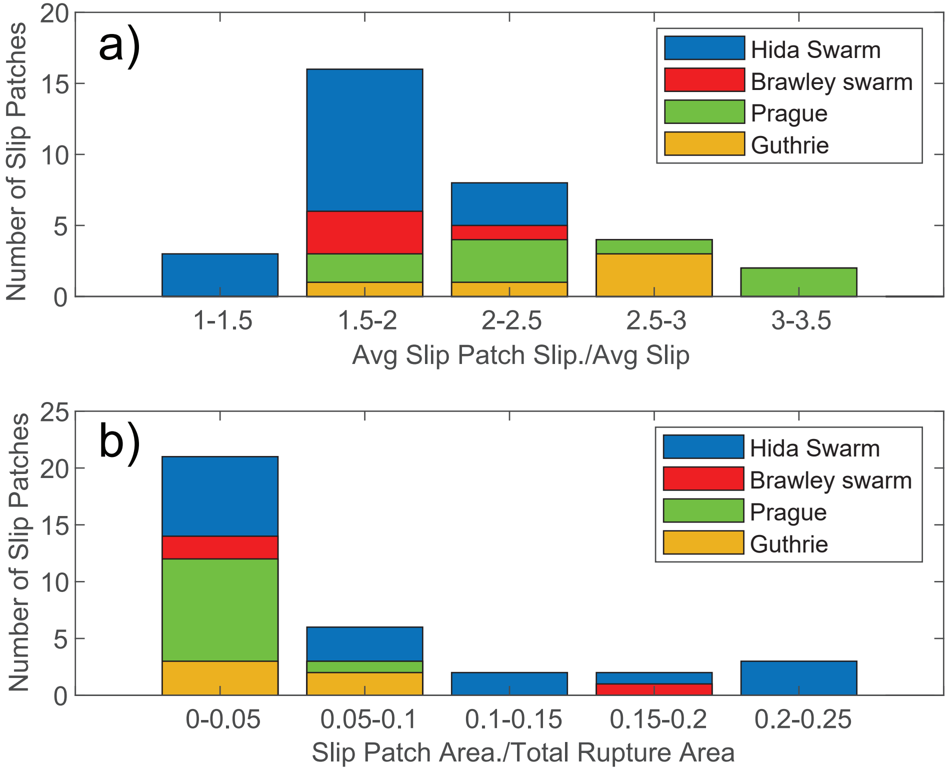

a)
Number of Slip Patches
20
15
10
5
0
Hida Swarm
Brawley swarm
Prague
Guthrie
1-1.5
1.5-2
2-2.5
2.5-3
3-3.5
Avg Slip Patch Slip./Avg Slip
b)
Number of Slip Patches
25
20
15
10
5
0
Hida Swarm
Brawley swarm
Prague
Guthrie
0-0.05
0.05-0.1
0.1-0.15
0.15-0.2
0.2-0.25
Slip Patch Area./Total Rupture Area